

Response of a Liquid ^3He Neutron Detector

A.E. Sharbaugh,^{a)} L. Jones,^{b)} and A.N. Villano^{c)}

*Department of Physics,
University of Colorado Denver,
Denver,
Colorado 80217,
USA*

(Dated: 29 December 2023)

Abstract. The $^3\text{He}(n,p)$ process is excellent for neutron detection between thermal and ~ 4 MeV because of the high cross section and near-complete energy transfer from the neutron to the proton. This process is typically used in gaseous forms with ionization readout detectors. Here we study the response of a liquid ^3He neutron detector with a scintillation readout. We anticipate an efficiency boost of around a factor of 64 compared to 10 atm gaseous detectors, given similar detector volumes.

INTRODUCTION

The (n,p) reaction occurs when a neutron enters the nucleus of an atom, simultaneously causing a proton to leave. This process provides a reliable method for measuring the neutron flux through a particular volume, provided that the cross section for the process is high enough and the Q-value is positive or not very negative. Furthermore, since in this process the outgoing proton carries an energy deterministically related to the incoming neutron energy, it is one of the only measurements that can measure *incoming* neutron energies unambiguously.

For our neutron detector design, we primarily utilize the reaction $^3\text{He}(n,p)^3\text{H}$ whose Q-value can be ascertained by subtracting the proton separation energy of ^4He from the neutron separation energy of the same. The separation energies are obtained from the most recent Atomic Mass Evaluation (AME) in 2020 [1, 2]. The resulting Q-value for the reaction $^3\text{He}(n,p)^3\text{H}$ is 763.755 keV. Our design differs from previous detectors using this process because those detectors were ^3He gas-based with typical fill pressures between 4–10 atm partial pressure of ^3He and equipped with ionization readouts [3, 4, 5]. Our design implements ^3He in the liquid state which is at least 64 times more dense [6] than the gas detectors mentioned (assuming a maximum ^3He partial pressure of 10 atm). The design has a scintillation readout via a traditional photomultiplier tube (PMT); silicon photomultipliers are frozen-out at the proposed operating temperatures.

Recently the SPICE/HeRALD collaboration provided a proof-of-principle for a cryogenic photomultiplier readout of a liquid helium volume [7]. The collaboration also kindly shared their published data with us in digital form which we use for our design. Our basic design is shown in Fig. 1. We have envisioned a hermetic copper vessel with a large gas space above a small cube ($2 \times 2 \times 2$ cm³) where liquid ^3He will collect when the vessel is filled with 6.63 liters (22.9 atm) of ^3He at room temperature and lowered to a temperature of 1 K. Liquification will be achieved by attaching the vessel to an off-the-shelf, commercially obtainable closed-cycle 1 K cryocooler [8]. The cubical portion of the vessel will have a small quartz window through coated with tetraphenyl butadiene (TPB) so the phototube can measure the helium scintillation [9].

There are two key applications that we had in mind when designing this neutron detector: measuring neutron backgrounds in the low-flux environments associated with rare event searches, and measurements of neutron-producing nuclear reactions with tiny cross sections. Rare event searches like dark matter and neutrinoless double-beta decay experiments are sensitive to neutron backgrounds and often operate deep underground to shield out as many neutrons as possible. Still, there are residual neutrons in the environment for various reasons [10]. The most common method used to estimate the level of the residual neutrons is by simulation: either of the (α ,n) process for radiogenic neutrons [11] or of cosmic rays for cosmogenic neutrons [12]. One key difficulty is that, while the simulations themselves have made great strides, there is often no measured spectrum to compare to because the neutron flux is so low that its measurement comes with large effort [5, 13]. We will focus the current study on the sensitivity of our detector design to neutrons in a deep underground environment (SNOLAB).

^{a)}Corresponding author: alya.sharbaugh@ucdenver.edu

^{b)}Electronic mail: luke.jones@ucdenver.edu

^{c)}Electronic mail: anthony.villano@ucdenver.edu

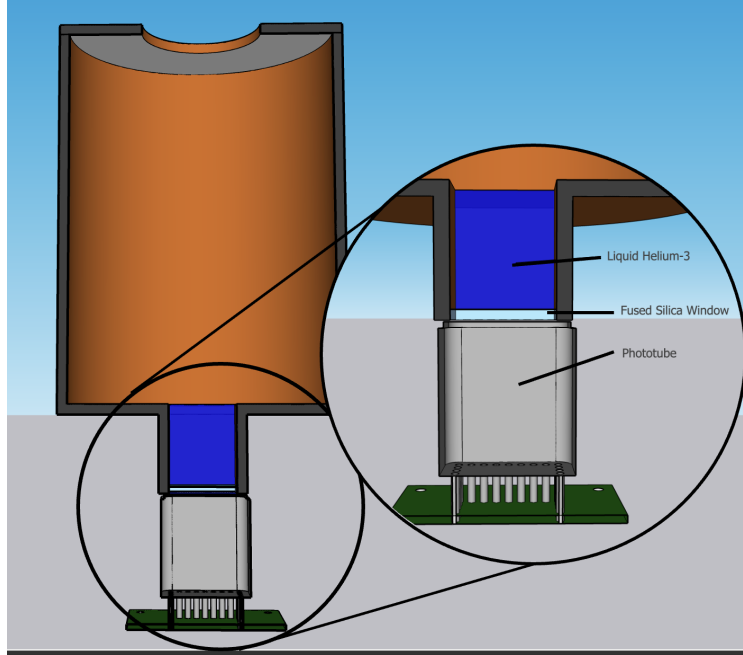


FIGURE 1: The prototype design of a liquid ^3He neutron detector with a photomultiplier readout. The height of the gaseous portion of the vessel is approximately 11 cm tall, whereas the liquid fills a $2 \times 2 \times 2 \text{ cm}^3$ cubical vessel attached near the bottom.

The measurements of neutron-producing nuclear reactions will not be discussed in detail but it is worth mentioning this as another application for our detector design and potentially critical to the field of nuclear astrophysics. Nuclear astrophysicists have sought for decades to understand the slow-neutron-capture process (s-process) in stars. The s-process is responsible for the production of almost half the heavy elements in the universe. In order to constrain this process hundreds of nuclear cross sections must be measured. One example of them is the $^{13}\text{C}(\alpha, n)^{16}\text{O}$ reaction, which serves as a neutron source in stars near the Gamow peak, between 150–230 keV. Current measurements for that region yield uncertainties of greater than 40% [14]. Another key example is the $^{22}\text{Ne}(\alpha, n)^{25}\text{Mg}$ which competes with the similar (α, γ) process that does not produce neutrons [15]. Each of those reactions have pico-barn level cross sections in the off-resonance regions and could be measured precisely with an instrument that has a high neutron detection efficiency.

SPECTRAL FEATURES OF $^3\text{HE}(\text{N}, \text{P})$

Beimer, et al. [3] outlines a procedure for computing the expected deposited-energy spectra when a monoenergetic neutron impinges on a gaseous ^3He detector cylinder of 5 cm diameter and 15 cm length. We have reproduced the Beimer model for all incident neutron energies by interpolating their measured spectral parameters. We are specifically interested in the proton leakage portion of the distribution. For liquid helium detectors—like the prototype we’re designing—we expect the response to be qualitatively similar except with substantially less proton leakage coming from the possibility of a proton escaping the sensitive area of the detector after the $^3\text{He}(\text{n}, \text{p})$ reaction.

In the Beimer reference, the response of the ^3He detector to neutrons was modeled by construction a probability distribution function (PDF) composed of elements from each of the physical processes involved. The processes were: elastic scattering from argon; elastic scattering from helium; proton leakage; and the (n,p) peak. The original reference used 17 parameters ($A_1 - A_{18}$; no A_{10}) to fit these key parts of the measured spectra to the response PDF, as seen in Fig. 2. The important portions of the spectrum for our purposes are the (n,p) peak, proton leakage, and elastic ^3He contribution, as we expect these processes to also be present in our liquid ^3He prototype.

The (n,p) peak is governed by the terms in Eq. 1. We define f_p to be the PDF of measured energy E for a neutron with energy E_n . Amplitude, A_1 and A_8 , behave similarly but the width of the Gaussian is different on the lower energy

side (A_3) than on the higher energy side (A_9). $Q=763.755$ keV represents the nuclear Q value for the ${}^3\text{He}$ (n,p) reaction discussed above.

$$f_p(E, E_n) = \begin{cases} A_1 e^{-\frac{1}{2} \left(\frac{(E_n+Q)-E}{A_3} \right)^2}; & E \leq (E_n + Q) \\ A_8 e^{-\frac{1}{2} \left(\frac{(E_n+Q)-E}{A_9} \right)^2}; & E > (E_n + Q) \end{cases} \quad (1)$$

The elastic ${}^3\text{He}$ contribution is governed by the terms in Eq. 2. This result depends implicitly on the incoming neutron energy E_n because the parameter A_{13} scales with this energy. The term $A_{13} - E$ gives a slightly negative slope at low energies. The remaining parameters in the numerator ensure the PDF is never negative for a given energy below the maximum recoil energy.

$$f_{ne}(E, E_n) = \frac{A_{11}(A_{13} - E) + A_{12}}{1 + e^{\frac{E-A_{13}}{A_{14}}}} \quad (2)$$

Parameters A_4 and A_6 describe the behavior of the exponential preceding the primary signal peak. The population of this region, shaded green or purple in Fig. 2, is determined by the number of protons which escape the active area and leak out of the detection medium. We define f_{esc} in Eq. 3. Note parameters A_2 and A_{10} are unused [3].

$$f_{esc}(E, E_n) = \frac{1}{2} \operatorname{erfc} \left(1 - \frac{(E_n + Q) - E}{A_3} \right) (A_1 A_4 e^{-\frac{(E_n+Q)-E}{A_5}} + A_6 e^{-\frac{(E_n+Q)-E}{A_7}}) \quad (3)$$

Based on our calculations, the leakage accounts for approximately 80% of the original peak. Protons (for 1.5 MeV incident neutrons) in gaseous detectors of this type have a stopping length of approximately 10 cm. The gaseous ${}^3\text{He}$ detectors used by Beimer et al. were cylindrical, with a diameter of 5 cm and a length of 15 cm, which led to many protons escaping. By contrast, protons in the proposed liquid ${}^3\text{He}$ detector are estimated to have a stopping length of no more than ~ 0.1 cm for up to around 2 MeV neutron energies. The liquid ${}^3\text{He}$ chamber will be a cube with dimensions $2\text{ cm} \times 2\text{ cm} \times 2\text{ cm}$. As a result, we anticipate only minor escape near the surfaces of the cube. Using the 0.1 cm stopping length as a thickness, this surface accounts for 27% of the total volume of the detector. We can further estimate that half of these interactions will rebound into the detector, resulting in an upper bound of 13.5% leakage. This assumption allows us to modify parameters A_4 and A_6 in our model. The complete probability distribution function (PDF) obtained by summing each equation can be seen in Fig. 2.

A notable efficiency boost between a gaseous detectors of Beimer and our designed liquid detector is expected. ${}^3\text{He}$ has higher density in the liquid state than in the gaseous state [6]. The density increase of the liquid ${}^3\text{He}$ detector we propose is a factor of 107, given a 6 atm fill pressure of the gaseous tube we compare to. The actual thickness of the gaseous detectors used by Beimer [3] were 5 cm thick, whereas our design is 2 cm thick; we therefore expect an efficiency gain of about $43 \times$ for neutrons going straight through the 5 cm dimension. This means that whereas Beimer [3] measured 0.03% and 0.02% peak efficiencies for their gaseous ${}^3\text{He}$ detectors at 1 MeV and 2.5 MeV neutron energies respectively, we would expect efficiencies of 1.5% and 0.88% respectively. For neutron energies of order 100 keV the Beimer gaseous detectors have measured efficiencies around 0.1% so we would expect at least a 4.4% efficiency. By understanding the parameters governing the ${}^3\text{He}$ (n,p) spectra, we can now extrapolate the model for cryogenic (~ 1 K) temperatures and assess the performance of the proposed liquid ${}^3\text{He}$ detector.

BERKELEY MODEL OF LIQUID ${}^4\text{He}$ RESPONSE

Recently it has been demonstrated by the SPICE/HeRALD collaboration at Berkeley that liquid ${}^4\text{He}$ can be used as a scintillation detector with low-temperature photomultipliers (PMTs) [7]. The Berkeley data show the response of liquid ${}^4\text{He}$ scintillation via PMT measurements at specific energies for electron recoil (ER) events (radiation that produces a recoiling electron in the detector medium) and events composed of nuclear recoils (NRs) of ${}^4\text{He}$ atoms. Since

our liquid ^3He prototype will utilize the (n,p) process we are primarily interested in proton recoil events whose behavior probably lies between the Berkeley data for electron and nuclear recoils. Nevertheless, we use these measurements as a starting point for the expected detector response in a ^3He scintillating liquid—assuming qualitative similarity to ^4He in terms of scintillation yield and resolution.

Our primary interest is to extrapolate this data, and predict the signal peak behavior of incident protons within the range of 700 keV - 3 MeV. To do so, we need to define certain characteristics of each signal peak. First, we fit a Gaussian curve to each signal peak in the Berkeley dataset (see Fig. 3 for an example). In total, we make 13 Gaussian fits (6 ER, and 7 NR). The fitting function is described by Equation 4.

$$G(x) = a_1 \exp\left(-\frac{1}{2} \left(\frac{x-a_2}{a_3}\right)^2\right) + a_4. \quad (4)$$

It should be noted that we obtain each data point from the same Gaussian curve with the exception of the point corresponding to 1090 keV NR. Instead, we fit this point to the following Gaussian plus linear curve denoted G_0 :

$$G_0(x) = a_1 \exp\left(-\frac{1}{2} \left(\frac{x-a_2}{a_3}\right)^2\right) + a_4 x + a_5, \quad (5)$$

the reason for this is that the fit to the other function was not particularly good in this case, so the new function allows for a more precise data point such that the uncertainty has a consistent order of magnitude relative to all other

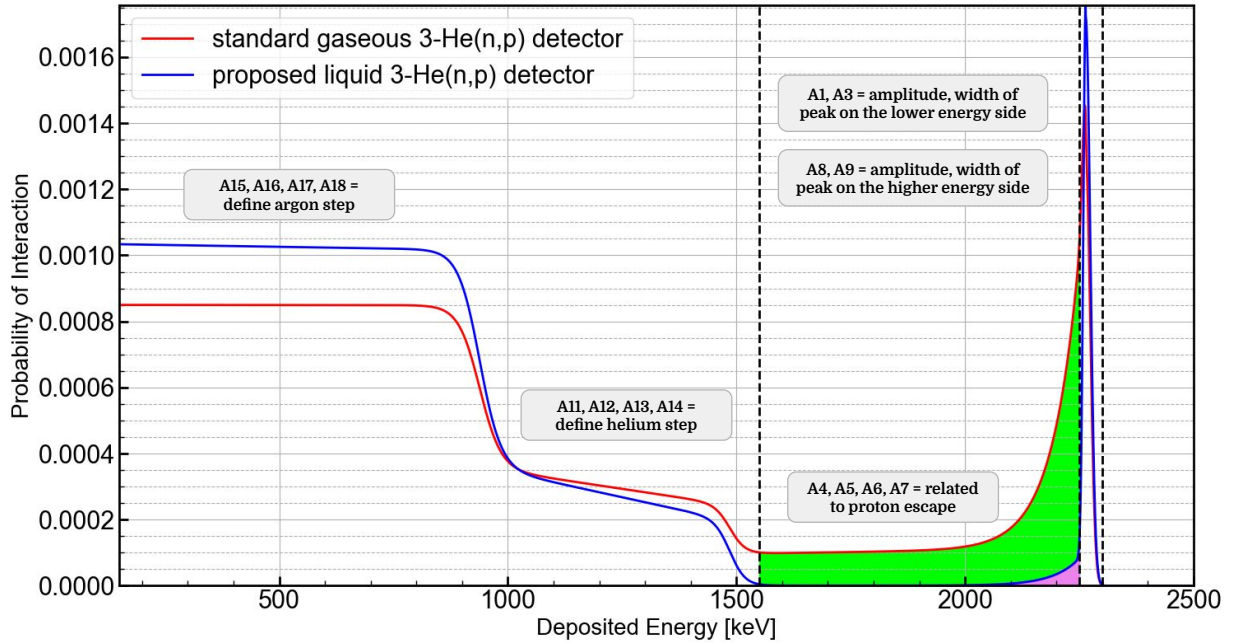


FIGURE 2: The parameters of the response function mapped to a 1.5 MeV signal peak. The red curve represents data collected by Biemer et al. using ionization vessels filled with a gaseous mixture containing a partial pressure of 6 atm of helium, 3 atm of argon, and 0.5 atm of methane [3]. Any scattering produced by the methane is negligible. Parameters $A_{11} - A_{14}$ describe the scattering step formed by the argon, but this part of the curve is not relevant to our analysis because the proposed detector will contain purely helium. The blue curve represents the predicted spectra for neutrons of $E_n=1.5$ MeV in the liquid ^3He detector. The area shaded green highlights the 80% leakage from the standard gaseous detector, while the area shaded purple highlights the 13.5% leakage from the proposed detector.

Reducing proton escape increases peak efficiency, resulting in a taller and narrower blue curve.

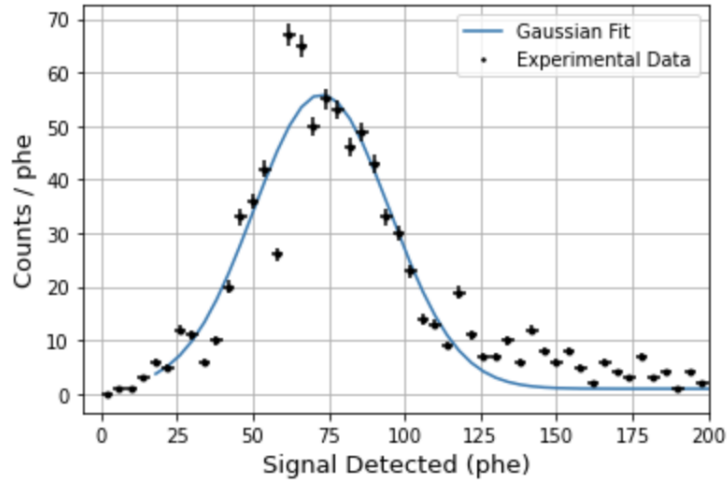


FIGURE 3: The experimental data is example data taken from [7], corresponding to 142 keV nuclear recoils. The horizontal represents the signal size in number of photoelectrons (phe), and the vertical represents counts per bin.

data points. Throughout all of these fits, the parameters we are interested in are a_2 and a_3 , as these determine the peak signal size and the width of our signal respectively, in number of photoelectrons (phe). After completing each fit, we have two sets of a_2 's and two sets of a_3 's, one for nuclear and one for electronic recoils. We then create a plot of each a_i vs. recoil energy E . The fits of these plots are outlined in Fig. 4.

For the a_2 's, we did a weighted fit to the collection of points to a linear function $y = mx + b$, where y is the signal size in npe, and x is the event energy in keV. The results of these linear fits using both our extracted yields and the Berkeley extracted yields are shown in Fig. 4, left sides.

For the a_3 parameters we model the overall behavior in a similar way, except using a weighted fit to a standard width-versus-energy function $y = \sqrt{Ax + \sigma_0^2}$. Again we do this fit for both our extracted widths and the ones from the Berkeley publication [7] and the results are displayed in Fig. 4. It was found that in all cases the σ_0 parameter was negligibly small, so we don't list it with our results. The reason for this is that we don't have data at low enough scattering energies to probe this baseline (zero-energy) resolution. After the fitting procedure, we end up with the parameters in Table I.

The fit parameters in Table I show rough agreement with the analysis of the Berkeley reference [7]. They likely differ because of the more precise fit function for each scattering histogram and a more careful treatment of systematic errors. We will use these models for the detector resolution in the next section despite the large extrapolation necessary (the highest fitted energy is around 1 MeV recoil for NRs and 180 keV for ERs whereas we need the detector performance at the \sim MeV scale for both NRs and ERs).

LIQUID ^3He WIDE-BAND NEUTRON SPECTRAL RESPONSE

We expect our liquid ^3He neutron detector design to be appropriate for low neutron flux environments because of its high efficiency relative to conventional gaseous ^3He tubes like those used by Beimer [3]. This is because of the much higher density of ^3He in the liquid state at 1 K— 0.0792 g/cm^3 —compared to a 6 atm gas with density $7.4 \times 10^{-4} \text{ g/cm}^3$ at room temperature [6]. In fact, our $2 \times 2 \times 2 \text{ cm}^3$ detector is expected register 3 times more neutron events above around 10 keV than the larger tubes (5 cm diameter; 15 cm length) of Beimer [3]. For typical gaseous tubes with fill pressures between 6–10 atm our design will be 64–107 times more efficient per volume at neutron energies larger than 10 keV. Below 10 keV the efficiency will quickly approach 100%.

SNOLAB is home to some of the most sensitive low-background experiments and as such has an exceptionally low neutron flux. We have estimated the neutron flux as a function of energy from around 6–10 MeV neutrons all the way down to thermal energies. These results are seen in Fig. 5. The high-energy flux is derived from the simulated neutron flux of the Super Cryogenic Dark Matter Search (SuperCDMS) for the SNOLAB environment [16]. In that

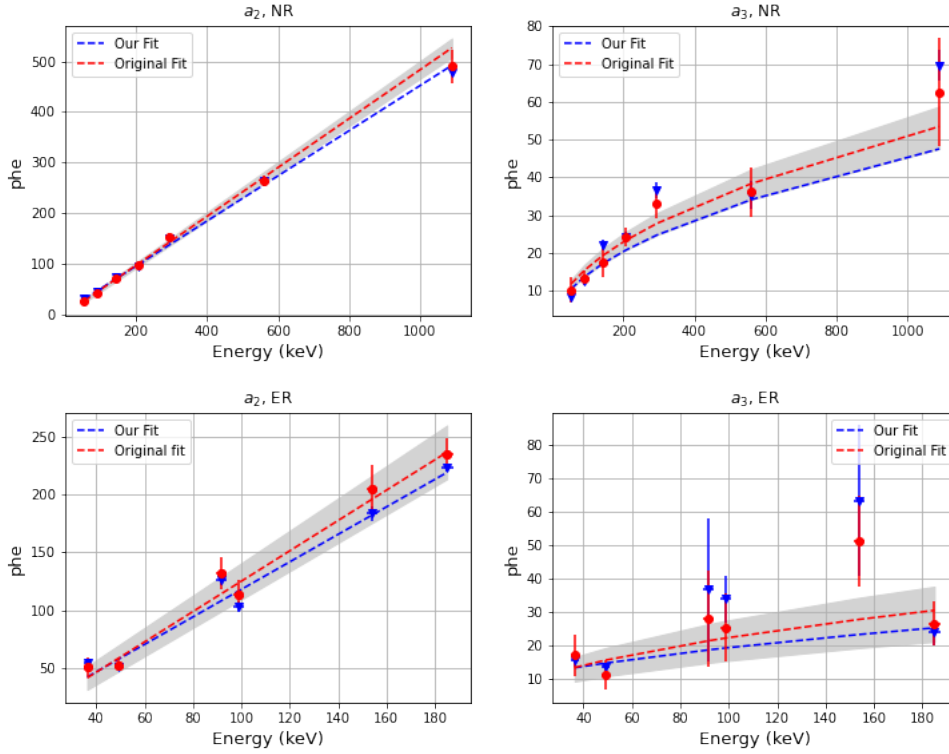


FIGURE 4: (Top) From left to right, the plots of a_2 and a_3 for nuclear recoils, respectively. (Bottom) From left to right, the plots of a_2 and a_3 for electronic recoils, respectively. For each figure, the energy uncertainties are obtained from [7] and the phe uncertainties are obtained from the covariance matrix of the fits. The red points correspond to the individual photon yield/width data and uncertainties from the Berkeley publication and the red dashed lines are fits to those points. The blue points represent the yield/widths from our Gaussian fits and their uncertainties and the blue dashed lines are a fit to those points. For each plot, we used the uncertainties from Table I to obtain an upper and lower bound for the energy behavior, denoted by the shaded regions centered around the red dashed line. Seeing as both the blue dashed line falls within this region for each plot, we see that the fits are consistent.

flux function there were several sharp features due to the modeling from SOURCES4C [17] and the propagation of (α, n) neutrons through the cavern rock and shotcrete. We have smoothed over features (see Fig. 5 red and purple curves) to produce a smooth flux function down to around 10 keV neutron energy. The normalization for the high-energy flux portion of this curve is taken from the SNOLAB handbook [18] where the value is 4000 n/m²/day. The high-energy flux is quoted as “fast” in the reference, this typically means above 1 MeV but no explicit lower bound is given. Below about 10 keV in neutron energy we have extrapolated the flux with a simple power-law function aE^b . The power law was determined by a linear regression of the log of our smoothed data in the range 10–20 keV. The extrapolated flux was joined at low energies with a Maxwell-Boltzmann distribution for (thermal) neutrons at room temperature. The unit-normalized function for the thermal neutrons is:

$$f_t(E) = 2\sqrt{\frac{E}{\pi}} \left(\frac{1}{kT}\right)^{3/2} \exp\left(-\frac{E}{kT}\right). \quad (6)$$

This thermal flux was multiplied by the measured total flux of thermal neutrons in SNOLAB [13], $4144.9 \pm 49.8 \pm 105.3$ n/m²/day. In this quoted measurement the first set of uncertainties is statistical and the second set is *systematic*. The systematic uncertainties come from inexactness in the analysis methods whereas the statistical uncertainties are based on the limited number of counts observed over the finite measurement period.

If the neutron flux as a function of energy from Fig. 5 is described as $f(E)$, then we might expect the overall rate in our detector to be $R = f(E)(\Sigma_{n,p} + \Sigma_e)V$, where R is the differential rate at a given neutron energy; $\Sigma_{n,p}$ is

Recoil Type	Slope	Intercept	A
NR	0.461 ± 0.003	4.310 ± 0.556	2.457 ± 0.192
ER	1.185 ± 0.023	-0.338 ± 1.610	3.109 ± 1.263

Recoil Type	Slope	Intercept	A
NR	0.483 ± 0.015	-0.202 ± 2.402	2.621 ± 0.548
ER	1.308 ± 0.087	-5.523 ± 6.998	5.052 ± 2.613

TABLE I: (Top) A table of fit parameters which quantify how the Gaussian parameters a_2 and a_3 behave with deposited energy according to our fits. (Bottom) A table of fit parameters which quantify how the Gaussian parameters a_2 and a_3 behave with deposited energy according to the fits from [7]. The 'slope' and 'intercept' parameters correspond to the slope and intercept of the a_2 plots. The parameter A corresponds to the non-linear fit function for the a_3 parameters. Again, we do not display values for the parameter σ_0 because they are all near zero. These plots are shown in Fig. 4

the macroscopic (n,p) cross section for ${}^3\text{He}$ as a function of neutron energy; Σ_e is the elastic cross section for ${}^3\text{He}$ as a function of neutron energy; and V is the detector volume. In fact this expression is only accurate for neutron energies above approximately 1 keV. Below that value the cross section for the (n,p) interaction is so large that there is significant *self-shielding*. Self-shielding occurs when a material has a high enough interaction probability that the neutrons will rarely penetrate to the center of the material. In the case of thermal neutrons (with energies around 0.025 eV) the situation is extreme and all (n,p) events will take place at the surface of the detector.

We modeled the neutron flux below 1 keV at the surface of our detector as non-zero only in the direction toward the inside of the detector in a 2π solid angle. This was accomplished by using the following *angular neutron flux* (following the notation of Duderstadt and Hamilton [19]):

$$\varphi(\mathbf{r}, E, \hat{\Omega}, t) = \frac{1}{4\pi} f(E) \theta(-\hat{\mathbf{n}} \cdot \hat{\Omega}), \quad (7)$$

where $\hat{\mathbf{n}}$ is the unit normal of the surface of our detector and θ is the unit step function. $\hat{\Omega}$ is the unit vector about point \mathbf{r} in which the flux is moving. The *angular current density* is then given by the following expression.

$$\mathbf{j}(\mathbf{r}, E, \hat{\Omega}, t) = \hat{\Omega} \varphi(\mathbf{r}, E, \hat{\Omega}, t) \quad (8)$$

Correspondingly, the rate of neutrons passing into our detector volume is:

$$R_{\text{surf}} = \oint \mathbf{j}(\mathbf{r}, E, \hat{\Omega}, t) \cdot dA dE d\hat{\Omega}. \quad (9)$$

Below 1 keV we have assumed that the detector is completely opaque and therefore the number of neutron detections is given by Eq. 9 independent of the macroscopic cross section $\Sigma_{n,p}$. This situation is depicted in Fig. 6. The left side shows how the flux is treated above 1 keV neutron energy—the detector is effectively transparent and the expression $f\Sigma V$ is an excellent approximation for the rate of detections. The right side of Fig. 6 shows that below 1 keV a neutron entering the detector is highly likely to interact near the surface, either right at the surface if the energy is very low (like thermal neutrons) or slightly further in. To assist the reader in understanding the transition between low neutron

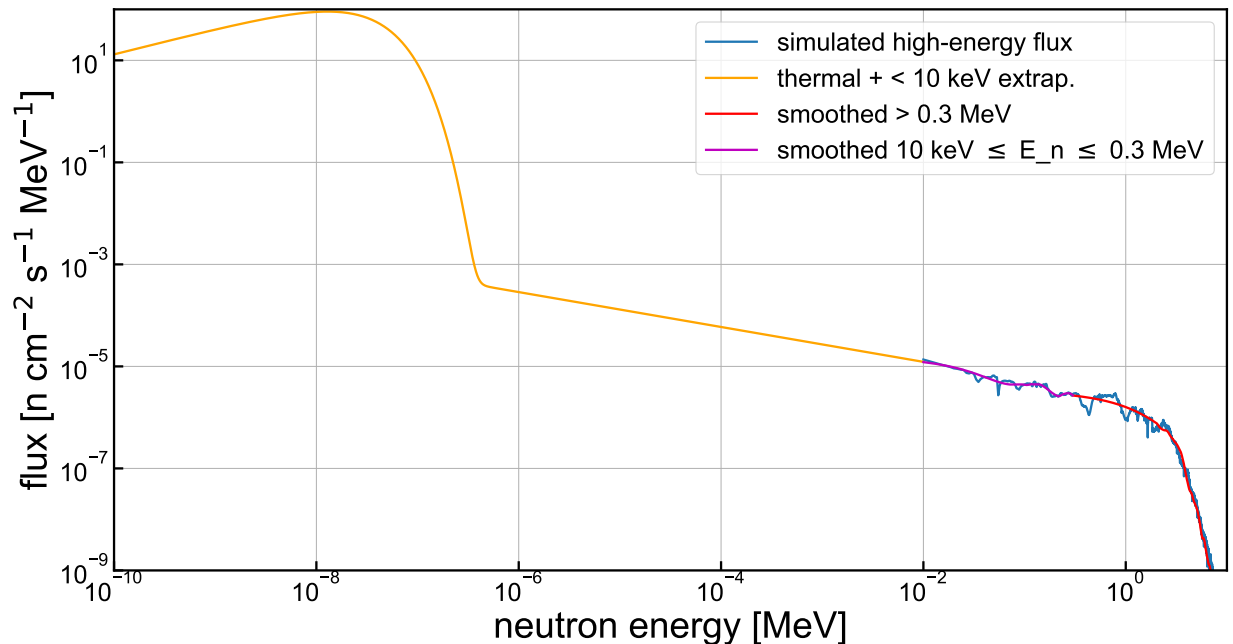


FIGURE 5: Neutron flux as a function of energy for the SNOLAB environment. The red and purple curves are smoothings of the high-energy neutrons computed from the SuperCDMS sensitivity projection paper [16]. The orange portion of the curve is an interpolation in the region below 10 keV down to the Maxwell-Boltzmann portion for the thermal neutron flux. The integral of the thermal flux region (from 10^{-4} eV to about 1 eV) is normalized to the measured underground SNOLAB thermal neutron flux: $4144.8 \pm 49.8 \pm 105.3$ n/m²/day.

mean free path and high mean free path, we have included a plot of the mean free path for neutrons in liquid and gaseous (6 atm partial pressure) ³He in Fig. ??a.

The (n,p) interactions which do take place near the edge of the detector—mostly, but not all below 1 keV—have a chance to have some of the proton energy escape the liquid. For gaseous detectors (as discussed earlier) this possibility could account for large percentages (up to 80%) of the measured events. Because of the higher densities in liquid this possibility is highly suppressed but can still happen. We computed, using the stopping power for protons in helium (obtained from the PSTAR online database version 2.0.1, July 2017 [20]), that 0.7% of low-energy events will have protons that “leak” out of the sensitive volume. We account for these in our model by selecting randomly that percentage of events in a given energy region and decreasing their deposited energy based on what percent of their stopping path is contained in the active region. To give the reader a sense for when leakage will happen we included the range of proton and alpha particles in ³He liquid and gas (at 6 atm pressure) in Fig. ??b.

For elastic scatters of neutrons on the ³He nuclei, the detector is always essentially transparent because the macroscopic elastic cross section Σ_{el} is small. Therefore elastic scattering does not modify the neutron flux throughout the detector and those scatters are modeled in the same way as our (n,p) interactions at high-energy (above 1 keV).

For both the (n,p) and elastic processes we use the evaluated cross sections as a function of energy from the JENDL 5.0 compilation [21]. From those, we calculate the needed macroscopic cross sections by scaling the cross section by the number density of the liquid ³He. The behavior of the cross sections is reflected in Fig. 7a.

Figure 8 shows the expected distribution of events for a $2 \times 2 \times 2$ cm³ detector of liquid ³He given the spectral model, anticipated scintillation resolutions, cross-section weighting, and leakage corrections previously discussed. We have used an NR detector response model for recoiling ³He and an ER response model for recoiling protons. This treatment is crude, but plausible: modeling ³He as NRs implicitly includes nuclear and electronic stopping powers, and the neglect of nuclear stopping power for protons is a good approximation for the initial recoil energies we are interested in (above around 764 keV). Our proton model is supported by Bethe-Bloch theory [22] where electronic stopping is dominant and dependent on the relativistic velocity β only. Most of our proton stopping happens between $\beta = 0.01$ and $\beta = 0.04$ (~ 764 keV)—within the range where electron-stopping Bethe-Bloch theory is adequate for the purposes of a rough (10–20% accurate) analysis of our design.

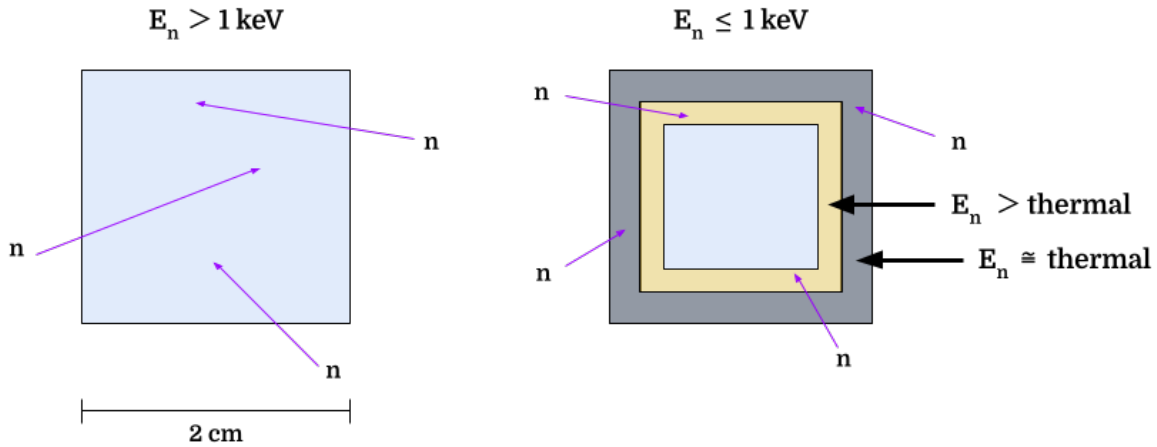


FIGURE 6: Schematic depicting how the flux is converted into an expected event rate. (Left) Shows situations where the (n,p) cross section is small enough (mean free path of neutrons much larger than detector size) that the flux can be treated as uniform throughout the detector and equal to the external neutron flux. (Right) Shows situations—taken to be $E_n < 1 \text{ keV}$ —where any incoming neutron is nearly guaranteed to produce an (n,p) reaction in the detector. The black region near the edge depicts the region where thermal neutrons ($E_n \sim 0.025 \text{ eV}$) are likely to interact. The tan region shows where neutrons of energies somewhat higher—up to around 1 keV—are likely to interact.

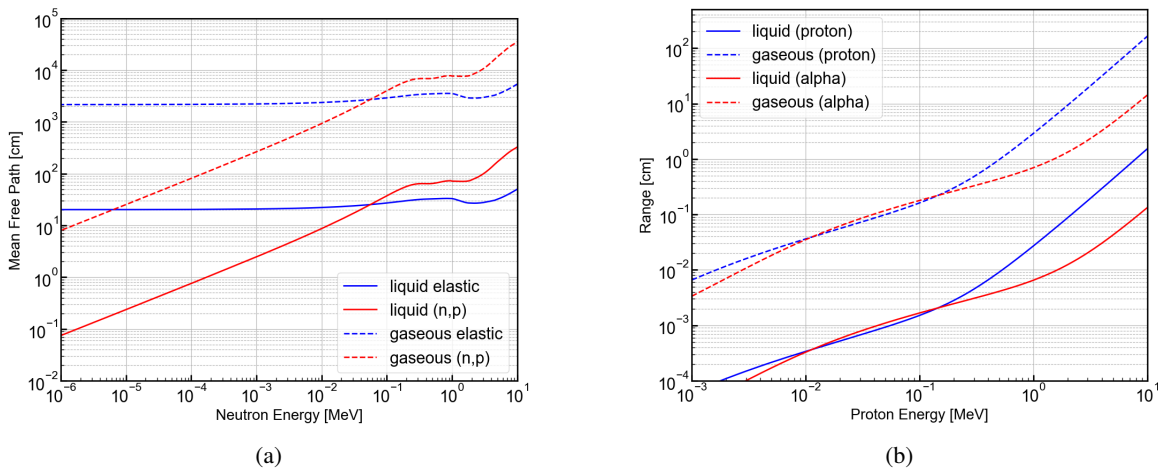


FIGURE 7: The properties of relevant particles as they travel in gaseous and liquid ^3He . (a) The mean free path of neutrons in ^3He for (n,p). Some neutrons will elastically scatter while others will react via the (n,p) process. (b) The range of protons and alpha particles in ^3He which help determine the area of an energy event after a neutron interaction.

The figure shows that for a 1 yr exposure we will produce an excellent measurement of the thermal neutron flux—given by the size of the peak near a deposited energy equal to the Q-value of the (n,p) reaction. It is also likely that a run period of that time will produce 3–4 counts in the high-energy neutron region above 2700 keV. Neutrons of those energies will constrain the overall fast flux present at the detector location. Similarly, the counts in the intermediate region, above around 266 keV neutron energy but below 1000 keV will create an important constraint in a region that has previously been difficult to measure.

CONCLUSIONS

While gaseous ^3He tubes are probably better for thermal neutron measurements due to their high surface area, our design is appropriate for cryogenic environments and above 1 keV in neutron energy our design surpasses gaseous tube performance. A single liquid ^3He detector of dimensions $2\times 2\times 2\text{ cm}^3$ has superior efficiency to a gaseous ^3He detector of the same dimensions for $\sim 1\text{ keV}$ – 4 MeV neutrons. Our current calculations also indicate that in a reasonable running period (1 yr) it can make impactful measurements in some of the lowest neutron flux environments in the world, like SNOLAB. Based on previous measurements at Berkeley [7] the resolution is expected to be useful for either low-flux measurements or nuclear physics beam measurements of neutrons.

Even though gaseous detectors are not very limited in size, scaling them will increase the radiogenic alpha background proportionally to the surface area. The Helium and Lead Observatory (HALO)—a gaseous ^3He array operating at SNOLAB—is a good comparison [23]. The array consists of 128 gaseous ^3He detectors of length 3 m or 2.5 m and 5 cm diameter at a partial pressure of 2.5 atm. Alpha backgrounds in this array are probably as low as can be expected for gas detectors, using a special ultra-pure nickel tubes that reach a thorium contamination of 1 ppt [24]. The large size of the array means while our prototype detector expects about 30 neutron events above 1 keV in one year, the HALO array will expect approximately 11,000. However, the alpha background is far lower in our liquid ^3He prototype because of the dramatically lower surface area and the possibility of ultra-pure copper. The thorium contamination has been demonstrated in copper as low as 0.01–0.03 ppt by the Majorana Demonstrator neutrinoless double-beta decay experiment [25]. The Enriched Xenon Observatory (EXO) has also demonstrated a contamination of thorium at 1.8 ppt for Quartz—the same material we will use for the PMT window [26]. Given those levels, we expect a signal-to-background ratio of 0.079 in HALO but between 4.62 and 15.42 in our small $2\times 2\times 2\text{ cm}^3$ prototype, depending on the copper purity (between 0.01 ppt and 1 ppt).

Our work indicates that this topic is worth further study. In particular, ambient gamma backgrounds must be considered as well as those that might originate from the instrumentation of our design—like from the photomultiplier

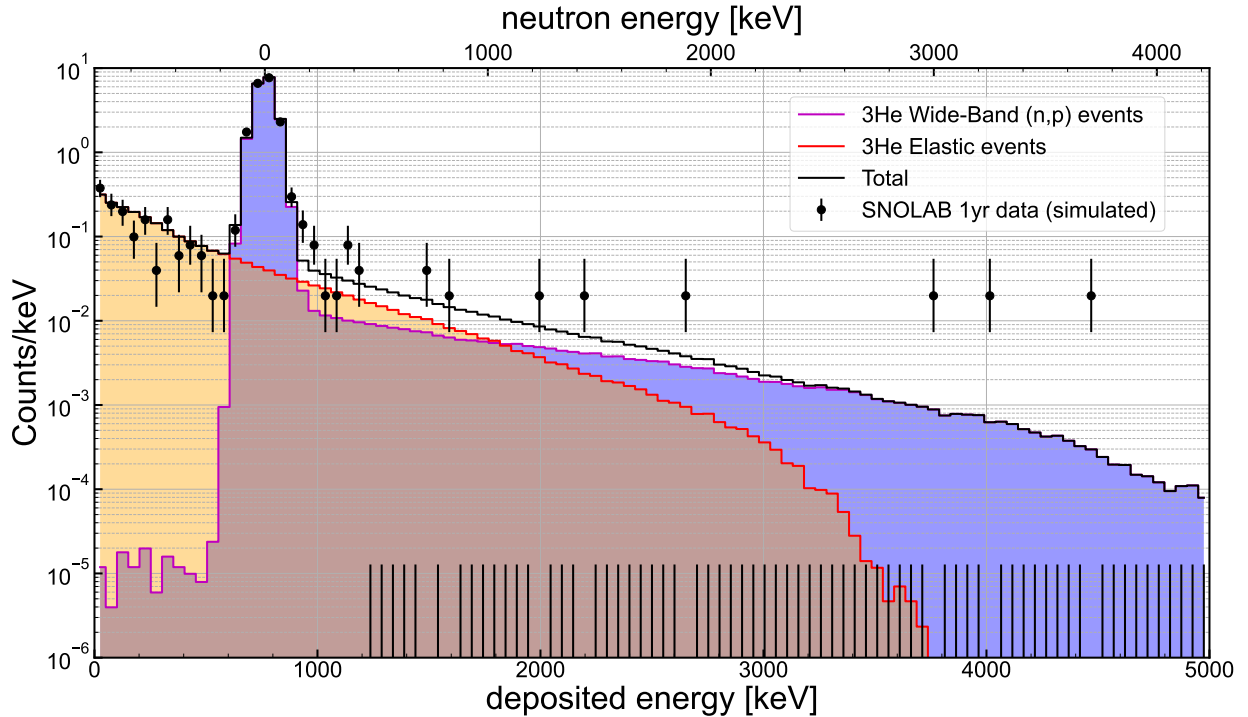


FIGURE 8: The expected spectrum of a $2\times 2\times 2\text{ cm}^3$ detector operated at SNOLAB for 1 yr (black points) compared to the expected total neutron distribution (black line) with (n,p) (blue shaded) and elastic (orange shaded) contributions. The uncertainties for zero-count bins were scaled so they did not obscure the plot, the points appear as black spikes on the plot ending at a vertical axis value of 10^{-5} .

tubes or electronics.

ACKNOWLEDGMENTS

The authors would like to thank Junsong Lin, A.J. Biffi, James deBoer, and Matt Pyle for helpful discussions. We also gratefully acknowledge the SPICE/HeRALD collaboration for providing us with the data from several plots in their paper.

REFERENCES

1. W. Huang, M. Wang, F. Kondev, G. Audi, and S. Naimi, "The ame 2020 atomic mass evaluation (i). evaluation of input data, and adjustment procedures*," *Chinese Physics C* **45**, 030002 (2021).
2. M. Wang, W. Huang, F. Kondev, G. Audi, and S. Naimi, "The ame 2020 atomic mass evaluation (ii). tables, graphs and references*," *Chinese Physics C* **45**, 030003 (2021).
3. K.-H. Beimer, G. Nyman, and O. Tengblad, "Response function for 3he neutron spectrometers," *Nuclear Instruments and Methods in Physics Research Section A: Accelerators, Spectrometers, Detectors and Associated Equipment* **245**, 402–414 (1986).
4. T. Langford, C. Bass, E. Beise, H. Breuer, D. Erwin, C. Heimbach, and J. Nico, "Event identification in 3he proportional counters using rise-time discrimination," *Nuclear Instruments and Methods in Physics Research Section A: Accelerators, Spectrometers, Detectors and Associated Equipment* **717**, 51–57 (2013).
5. A. Best *et al.*, "Low energy neutron background in deep underground laboratories," *Nuclear Instruments and Methods in Physics Research Section A: Accelerators, Spectrometers, Detectors and Associated Equipment* **812**, 1–6 (2016).
6. E. C. Kerr, "Orthobaric densities of he³ 1.3°k to 3.2°k," *Phys. Rev.* **96**, 551–554 (1954).
7. A. Biekert *et al.* (SPICE/HeRALD Collaboration), "Scintillation yield from electronic and nuclear recoils in superfluid ⁴He," *Phys. Rev. D* **105**, 092005 (2022).
8. Cryomech, "Closed-Cycle 1L Cryocooler," <https://www.cryomech.com/articles/closed-cycle-1k-cryocooler/>, online; accessed 26 June 2023.
9. D. McKinsey *et al.*, "Fluorescence efficiencies of thin scintillating films in the extreme ultraviolet spectral region," *Nuclear Instruments and Methods in Physics Research Section B: Beam Interactions with Materials and Atoms* **132**, 351–358 (1997).
10. N. Dokania *et al.*, "Study of neutron-induced background and its effect on the search of Onbb decay in 124sn," *Journal of Instrumentation* **9**, P11002 (2014).
11. J. Cooley, K. Palladino, H. Qiu, M. Selvi, S. Scorza, and C. Zhang, "Input comparison of radiogenic neutron estimates for ultra-low background experiments," *Nuclear Instruments and Methods in Physics Research Section A: Accelerators, Spectrometers, Detectors and Associated Equipment* **888**, 110–118 (2018).
12. D.-M. Mei and A. Hime, "Muon-induced background study for underground laboratories," *Phys. Rev. D* **73**, 053004 (2006).
13. M. Browne, *Preparation for Deployment of the Neutral Current Detectors (NCDs) for the Sudbury Neutrino Observatory*, Ph.D. Dissertation (1999).
14. G. F. Ciani *et al.* (LUNA Collaboration), "Direct measurement of the ¹³C(α, n)¹⁶O cross section into the s-process gamow peak," *Phys. Rev. Lett.* **127**, 152701 (2021).
15. M. Wiescher, R. J. deBoer, and J. Görres, "The resonances in the 22Ne+alpha fusion reactions," *The European Physical Journal A* **59**, 11 (2023).
16. R. Agnese *et al.* (SuperCDMS Collaboration), "Projected sensitivity of the supercdms snolab experiment," *Phys. Rev. D* **95**, 082002 (2017).
17. W. B. Wilson *et al.*, "Sources 4c: a code for calculating (α, n), spontaneous fission, and delayed neutron sources and spectra," Tech. Rep. (United States, Jan 2002) IA-UR-02-1839.
18. "Snolab users handbook rev. 2," Tech. Rep. (2006).
19. J. Duderstadt and L. Hamilton, *Nuclear Reactor Analysis* (Wiley, 1976).
20. M. Berger, J. Coursey, and M. Zucker, "Estar, pstar, and astar: Computer programs for calculating stopping-power and range tables for electrons, protons, and helium ions (version 2.0.1)." Tech. Rep. (National Institute of Standards and Technology, Gaithersburg, MD., Jul 2017).
21. O. Iwamoto *et al.*, "Japanese evaluated nuclear data library version 5: Jendl-5," *Journal of Nuclear Science and Technology* **60**, 1–60 (2023), <https://doi.org/10.1080/00223131.2022.2141903>.
22. P. A. Zyla *et al.* (Particle Data Group), "Review of Particle Physics," *PTEP* **2020**, 083C01 (2020), pp. 536–538.
23. C. Bruulsema, *Calibration and commissioning of the Helium and Lead Observatory*, Master's Thesis (2017).
24. J. Boger *et al.*, "The sudbury neutrino observatory," *Nuclear Instruments and Methods in Physics Research Section A: Accelerators, Spectrometers, Detectors and Associated Equipment* **449**, 172–207 (2000).
25. N. Abgrall *et al.*, "The majorana demonstrator radioassay program," *Nuclear Instruments and Methods in Physics Research Section A: Accelerators, Spectrometers, Detectors and Associated Equipment* **828**, 22–36 (2016).
26. D. Leonard *et al.*, "Systematic study of trace radioactive impurities in candidate construction materials for exo-200," *Nuclear Instruments and Methods in Physics Research Section A: Accelerators, Spectrometers, Detectors and Associated Equipment* **591**, 490–509 (2008).